Simulating Local Buckling-Induced Softening in Steel Members Using an Equivalent Nonlocal Material Model in Displacement-Based Fiber Elements

Subodh Kolwankar, S.M.ASCE[1]; Amit Kanvinde, M.ASCE[2]; Maha Kenawy, S.M.ASCE[3]; Dimitrios Lignos, M.ASCE[4]; and Sashi Kunnath, F.ASCE[5]

Abstract: Fiber-based elements are commonly used to simulate steel beam–columns because of their ability to capture *P-M* interactions and spread of plasticity. However, when mechanisms such as local buckling result in effective softening at the fiber scale, conventional fiber models exhibit mesh dependence. To address this, a two-dimensional (2D) nonlocal fiber-based beam–column model is developed and implemented numerically. The model focuses on hot-rolled wide flange sections (W-sections) that exhibit local buckling-induced softening when subjected to combinations of axial compression and flexure. The formulation upscales a previously developed nonlocal formulation for single-fiber buckling to the full frame element. The formulation incorporates a physical length scale associated with local buckling along with an effective softening constitutive relationship at the fiber level. To support these aspects of the model, 43 continuum finite element (CFE) test problems are constructed. These test problems examine a range of parameters, including the axial load, cross section, and moment gradient. The implemented formulation is validated against CFE models as well as physical steel beam–column experiments that exhibit local buckling-nduced softening. The formulation successfully predicts postpeak response for these validation cases in a mesh-independent manner, while also capturing the effects of P-M interactions and moment gradient. To enable convenient generalization, guidelines for calibration and selection of the model parameters are provided. Limitations are discussed along with areas for future development. **DOI: 10.1061/(ASCE)ST.1943-541X.0002189.** © *2018 American Society of Civil Engineers.*

Author keywords: Fiber models; Localization; Nonlocal formulations; Frame elements.

Introduction

Extreme limit states, such as earthquake- or blast-induced collapse in steel-framed structures, are precipitated by a loss of component strength at high deformations. In rolled steel beam–columns, local buckling is often the mechanism responsible for strength loss (others causes being lateral-torsional buckling and fracture). Fig. 1 schematically shows a rolled steel beam–column subjected to flexure, illustrating flange local buckling within the plastic hinge region. As indicated in the figure, a strongly geometric nonlinear response within the buckling zone results in negative stiffness at the component level (Hamburger et al. 2009). While loss of component strength is one outcome of this negative stiffness, localization of deformation in the buckling zone is another. Localization of deformation ultimately leads to fracture through plastic strain amplification. Research indicates that simulating this postpeak response is critical for accurate structural performance assessment. For example, Ibarra and Krawinkler (2005) show that postpeak negative stiffness is a dominant parameter controlling the seismic collapse of steel-framed structures, and Fell et al. (2010) indicate that the continuum plastic strain within the local buckle triggers ductile fracture in steel braces. The postlocal buckling response can be simulated accurately through large-deformation elastoplastic continuum finite element (CFE) simulations, in which material response is represented as monotonically hardening, supplemented by direct simulation of the geometric nonlinear effects that give rise to negative stiffness (for example, see Fogarty and El-Tawil 2015; Elkady and Lignos 2015). However, line-element-based models using beam–column frame elements remain a popular choice for structural performance assessment in most practical and research settings. This can be attributed to their computational efficiency, which (despite rapid advances in computing hardware) is increasing in importance as emerging trends in structural performance and reliability assessment [FEMA P-58 (FEMA 2012); NIST 2010] mandate computationally onerous suites of parametric simulations.

Despite their computational efficiency, line elements have significant limitations, especially when simulating postpeak response. To describe the limitations of line elements, it is useful to classify line-element-based approaches as either concentrated plasticity, plastic hinge elements (see Dides and de la Llera 2005 for a comprehensive review), or distributed-plasticity elements (Spacone and Filippou 1996). Distributed-plasticity elements may be further classified as force-based versus displacement-based. Fiber elements are a specific instance of distributed-plasticity elements in which stress resultants and deformations are determined at the cross-sectional (rather than continuum) level. Plastic hinge models

[1]Graduate Research Assistant, Dept. of Civil and Environmental Engineering, Univ. of California, Davis, CA 95616.

[2]Professor, Dept. of Civil and Environmental Engineering, Univ. of California, Davis, CA 95616 (corresponding author). Email: kanvinde@ucdavis.edu

[3]Graduate Research Assistant, Dept. of Civil and Environmental Engineering, Univ. of California, Davis, CA 95616.

[4]Associate Professor, Dept. of Architecture, Civil, and Environmental Engineering, Ecole Polytechnique Fédérale de Lausanne, Lausanne CH-1015, Switzerland.

[5]Professor, Dept. of Civil and Environmental Engineering, Univ. of California, Davis, CA 95616.

Note. This manuscript was submitted on October 9, 2017; approved on May 3, 2018; published online on July 31, 2018. Discussion period open until December 31, 2018; separate discussions must be submitted for individual papers. This paper is part of the ***Journal of Structural Engineering***, © ASCE, ISSN 0733-9445.

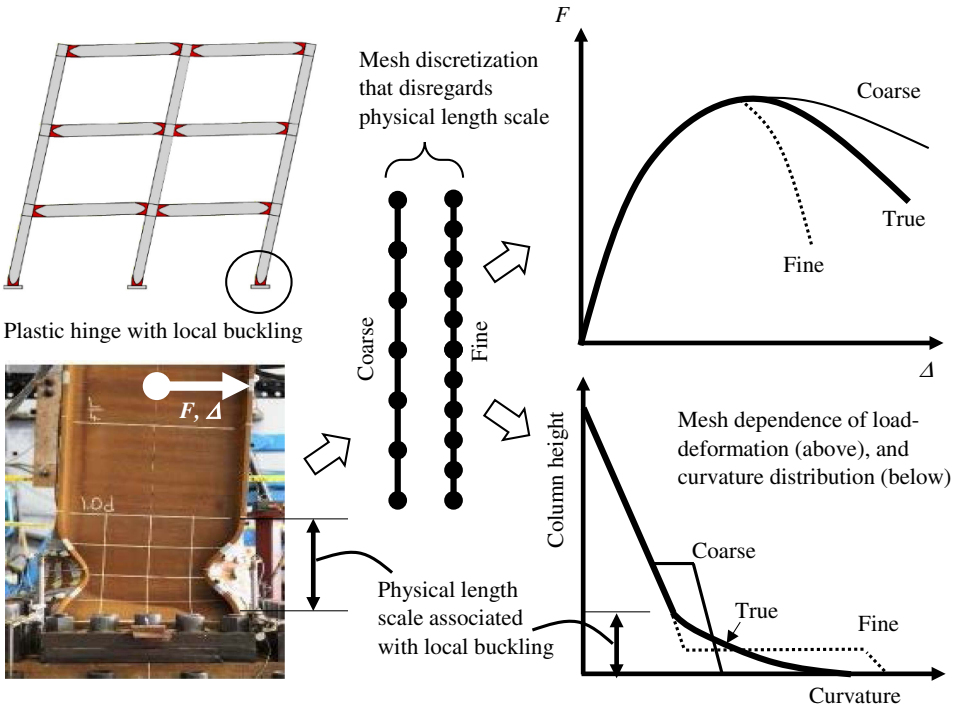

Fig. 1. Problem and causes of mesh dependence in rolled steel members with local buckling.

require calibration to component tests (i.e., they cannot be conveniently generalized from material tests), do not simulate spread of plasticity, and require a priori placement of plastic hinges, disallowing simulation of yielding in arbitrary locations. Moreover, although theoretically possible, concentrated plasticity models do not typically capture axial force-moment ($P-M$) interaction. Fiber elements rely on uniaxial stress–strain response at a fiber cross-sectional level, enabling simulation of plasticity in arbitrary locations, spread of plasticity, $P-M$ interaction, and, perhaps most importantly, generalization of properties from material (rather than component) tests. However, for simulating postpeak response, fiber elements are susceptible to problems when softening constitutive models are used to represent postbuckling response. Specifically, postpeak response (both negative stiffness and curvature distribution) predicted by fiber elements is susceptible to severe mesh dependence or nonobjectivity (Coleman and Spacone 2001; Wu and Wang 2010; Sideris and Salehi 2016). It is relevant to note here that such mesh dependence is not a peculiarity of fiber elements, but occurs even in CFE simulations when softening constitutive models are used. Nonetheless, unlike fiber models, CFE models offer a convenient way to simulate postbuckling response without the use of softening constitutive laws. The implication is that such nonobjectivity is usually more difficult to overcome in fiber models. Fig. 1 illustrates this nonobjectivity, in which the negative stiffness in any element (or mesh unit, such as Gauss point spacing, which is commonly used in fiber elements) localizes strains in that unit, unloading the neighboring intervals. Thus, Gauss point spacing (or mesh size) acts as an arbitrary length scale, controlling the strain distribution and global load-deformation response. This type of mesh dependence due to softening is a well-studied phenomenon (Engelen et al. 2003; Jirásek and Rolshoven 2003; Bazant and Jirasek 2002) in the context of material softening in CFE simulations. This mesh dependence arises from the singular nature of the analytical solution when softening constitutive models are used without an accompanying physical length scale; the solution converges to this singular solution as the mesh is refined. Introducing a physical regularizing length scale into the simulation (if done appropriately) has the potential to mitigate this mesh dependence, by distributing strains over a region defined by the length scale. Analogous research for fiber-based frame elements is not as extensive (examples include Pugh et al. 2015; Valipour and Foster 2009; Salehi and Sideris 2017; Zhang and Khandelwal 2016; Khaloo and Tariverdilo 2002, 2003). As a consequence, popular commercial (e.g., PERFORM-3D, ETABS; Computers and Structures 2016) and research (e.g., OpenSees version 2.5.0) codes still utilize fiber elements that are not regularized in any manner and suffer from pathological mesh dependence. For frame elements, the regularizing length scale may be introduced by coordinating the mesh size with the softening/negative slope of the constitutive model to produce acceptable load-deformation response. For example, Coleman and Spacone (2001) used the fracture energy to regularize the constitutive law, based on concepts developed by Bazant and Oh (1983) and Bazant and Planas (1998). Although this approach expediently mitigates mesh dependency in load-deformation response, it still generates localized strain and curvature distributions. Nonlocal formulations enrich the strains by explicitly introducing a length scale (examples include Salehi and Sideris 2017 and Zhang and Khandelwal 2016), wherein the nonlocal strain at any location is computed from strains at neighboring locations as a weighted average. In continuum modeling, the use of nonlocal approaches and the inclusion of a material-dependent length scale is well-established. Examples include the simulation of material damage or deterioration [e.g., crushing in concrete (di Prisco and Mazars 1996) or shear banding in geomaterials (Shuttle and Smith 1988)]; correspondingly, the length scales reflect material morphological features and heterogeneities that are otherwise not simulated in continuum models, such as aggregate size in concrete (Bazant 1976). In contrast, softening and localization (at the component scale) in rolled steel members is often triggered by three-dimensional geometric nonlinear phenomena such as local buckling, for which length scales have physical basis in these phenomena (such as thebuckle wavelength—see Fig. 1).

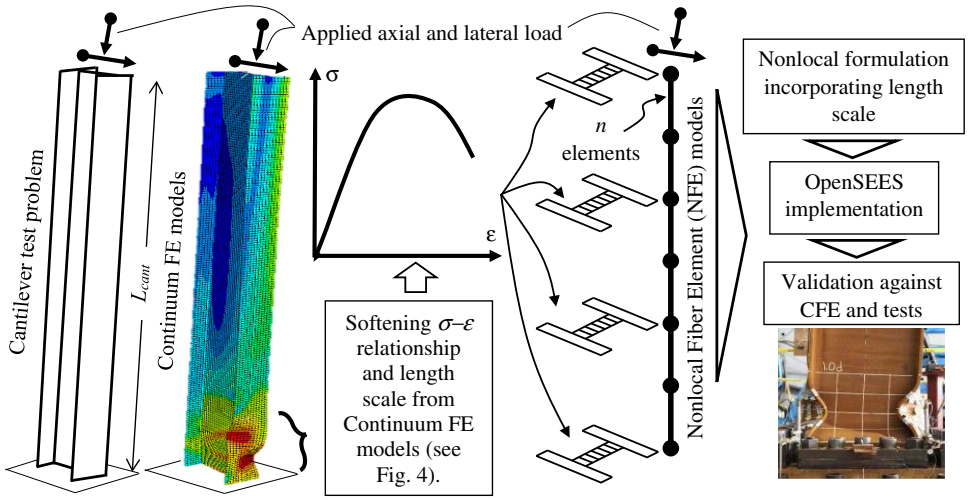

Fig. 2. Schematic illustration of research methodology and components.

Other sources of component-scale softening in steel members include global buckling, lateral-torsional buckling, or ductile tearing. Common approaches for the simulation of local buckling (which is the focus of this paper) within fiber elements include (1) simulating the softening in a local constitutive manner, disregarding mesh sensitivity entirely, with serious loss of accuracy and objectivity at extreme limit states, (2) using the approaches for mesh adjustment outlined previously, which also result in localized strains and curvatures, or (3) using concentrated plastic hinge formulations, which mitigate nonobjectivity but are deficient in other ways—that is, they cannot simulate plasticity at arbitrary locations or distributed plasticity, are not facile with respect to the simulation of $P-M$ interaction, and require component (rather than material) tests for calibration.

Recent work by the authors (Kolwankar et al. 2017) demonstrated that an integral-based nonlocal formulation is able to successfully mitigate buckling-induced mesh dependence in a steel bar represented as a single fiber, while also reproducing the strain distribution within the localized (buckled) zone. This is promising in relation to the above discussion, because this single-fiber formulation provides a basis for extension to a full fiber-based beam–column element. Motivated by this, the specific objectives of this paper are (1) to present a 2D fiber beam–column element formulation to simulate rolled steel W-sections subjected to monotonic flexural/axial load that uses a nonlocal approach to mitigate the mesh dependence of the postpeak response, (2) to present a method for determining the characteristic length corresponding to local buckling as an input to the nonlocal approach, (3) to describe the numerical implementation of the model with guidelines for calibration and usage, and (4) to evaluate this implemented formulation against CFE as well as test data. The paper begins by articulating the scope of the problem and the scientific methodology. Subsequent sections describe individual components of this methodology; these include the nonlocal formulation itself and characterization of its various aspects, including length scales and softening constitutive response, using CFE simulations. This is followed by a brief discussion of the numerical implementation within OpenSees and validation of the approach against CFE simulations and physical experiments. The paper concludes by providing guidelines for usage and discusses limitations of the approach and its implementation.

Methodology and Components of Research

Fig. 2 schematically illustrates the main components of the research methodology. Referring to the figure, the target application was rolled steel beam–columns (e.g., in moment-resisting frames) subjected to inelastic bending coupled with axial force demands. Given this, a suite of 43 test problems was developed. Each test problem involved a cantilever column with properties and loading conditions summarized in Table 1; among these, simulations 41–43 were complementary to columns physically tested by Lignos et al. (2016). In addition to its geometric simplicity and determinacy, the cantilever column enabled effective interrogation of four key variables that are critical from the perspective of moment frame simulation: cross-sectional shape, axial load ratio (the fraction of the yield strength, expressed as P/P_y), moment gradient (denoted as the moment-shear ratio M:V), and manner of loading

Table 1. Test problems (i.e., simulation matrix) and parameters

Test problem number	Section	$b_f/2t_f$	h/t_w	M:V (mm)[a]	P/P_y	Loading
1–3	W27X161	6.48	38.55	4,500	0, 0.2, 0.5	NP[b]
4–6	W27X161	6.48	38.55	2,250	0, 0.2, 0.5	NP
7–8	W27X161	6.48	38.55	4,500, 2,250	0.5	P[b]
9–11	W27X84	7.81	55.26	4,500	0, 0.2, 0.5	NP
12–14	W27X84	7.81	55.26	2,250	0, 0.2, 0.5	NP
15–16	W27X84	7.81	55.26	4,500, 2,250	0.5	P
17–19	W24X146	5.92	34.65	4,500	0, 0.2, 0.5	NP
20–22	W24X146	5.92	34.65	2,250	0, 0.2, 0.5	NP
23–24	W24X146	5.92	34.65	4,500, 2,250	0.5	P
25–27	W24X68	7.67	54.29	4,500	0, 0.2, 0.5	NP
28–30	W24X68	7.67	54.29	2,250	0, 0.2, 0.5	NP
31–32	W24X68	7.67	54.29	4,500, 2,250	0.5	P
33–35	W21X48	9.47	56.40	4,500	0, 0.2, 0.5	NP
36–38	W21X48	9.47	56.40	2,250	0, 0.2, 0.5	NP
39–40	W21X48	9.47	56.40	4,500, 2,250	0.5	P
41–43	W16X89[c]	5.94	28.67	1,875	0, 0.3, 0.5	NP

[a]M:V represents the moment gradient, also equal to length of cantilever model.
[b]Nonproportional and proportional loading.
[c]Complementary to experiments by Lignos et al. (2016).

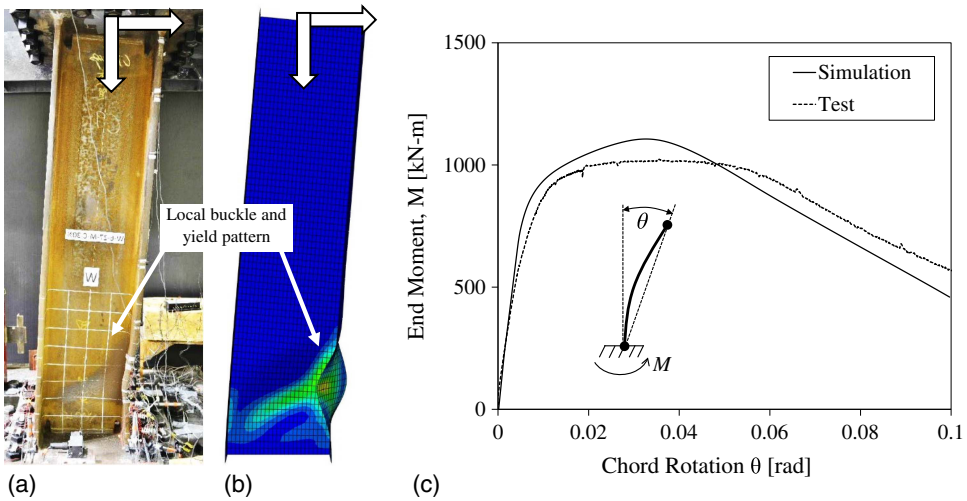

Fig. 3. Representative comparison between results from experiments (W16X89, $P/P_y = 0.3$) and continuum finite element simulations: (a) test specimen postlocal buckling at 8% chord rotation; (b) simulation at 8% chord rotation; and (c) load deformation curve.

(i.e., nonproportional—with the axial load introduced prior to lateral deformation, or proportional—in which both loads are introduced simultaneously). The values of these parameters (also summarized in Table 1) and the cantilever lengths of the column ($L = M{:}V$, defining the moment gradient) were selected to encompass commonly occurring conditions in seismic design and response (Elkady and Lignos 2015). For each test problem, two simulation models (both illustrated schematically in Fig. 2) were constructed:

- A continuum finite element model in the commercial platform ABAQUS version 6.14-1. Validated against experimental data by Lignos et al. (2016), this model provides qualitative and quantitative insights into the modes of local buckling to inform the nonlocal formulation for the line element model. This includes buckling shapes, deformation and strain patterns, localization length and its variation over the cross section, and effective stress–strain response of the buckling portions of the cross section. In addtion, the CFE models provide a calibration and validation dataset for the line element model.
- A nonlocal strain-enabled fiber-based line element model in the platform OpenSees version 2.5.0: Referring to Fig. 2, this nonlocal fiber element (NFE) model consists of n displacement-based beam–column elements (with cubic shape functions) connected serially, wherein n may be varied parametrically. For the NFE model (1) the element cross section is discretized into fibers; the web is discretized into fibers of 12.5×12.5 mm, whereas each flange is a single fiber, (2) strains at any point in the cross section may be determined from curvatures based on the plane-sections-remain-plane (PSRP) assumption, (3) stress resultants at the cross section (i.e., axial forces and moments) are determined by integrating stresses in individual fibers, and (4) element end forces are determined through the principle of virtual displacements by integrating cross-sectional forces determined at five Gauss points along the length. The model has the ability to assign any constitutive model to any of the fibers. However, in a departure from conventional fiber models, the NFE model allows computation of nonlocal strain at any Gauss point within any fiber by operating on strains from neighboring Gauss points and even neighboring elements. The NFE models constructed as previously discussed provide the numerical infrastructure for implementing the nonlocal formulation. This comprises the following steps, executed sequentially:

1. Recovery of information from the CFE simulations that may be used to inform the NFE models; this includes buckled shape profiles, localization length and its cross-sectional variation, stress–strain response over these localized regions, and corresponding load deformation response. Since these simulations have been validated by test data to represent physical phenomena associated with local buckling, information obtained from them may be considered true responses for the purposes of benchmarking the NFE models.
2. Development of a nonlocal formulation that is able to represent local buckling response based on the benchmark response obtained from the CFE simulations (in Step 1) and the prior formulation for single-fiber element buckling (Kolwankar et al. 2017).
3. Implementation of this formulation within the NFE model in OpenSees in a manner that allows for user-friendly simulation of frame structures with local buckling-induced softening and localization.
4. Assessment of the implemented formulation against experimental data and CFE benchmark response and development of guidelines for the calibration and use of this implemented formulation.

Continuum Finite Element Models of Beam Columns

The CFE simulations provided benchmark data for the local buckling response of beam–columns under bending and axial load. To this end, the CFE models reproduced aspects of physical response that control local buckling, namely large deformations and nonlinear elastoplastic response. Fig. 3(a) illustrates a deformed mesh (showing contours of plastic strain) of a CFE simulation for test problem 42 (W16x89, $P/P_y = 0.3$, $M{:}V = 1{,}875$ mm; see Table 1). To construct these models, protocols developed by Elkady and Lignos (2015) were used. These models utilized shell elements (four-node reduced integration; S4R in ABAQUS). Each model was meshed using element size on the order of 25×25 mm. Mesh convergence studies by Elkady and Lignos (2015) indicate that this level of mesh refinement is able to appropriately represent stress gradients due to local buckling. Initial imperfections were introduced into the model as perturbations to initiate local buckling.

The size and shape of these imperfections was based on procedures developed by Elkady and Lignos (2015). The constitutive response of the material was represented through a von Mises yield surface, supplemented by combined isotropic-kinematic hardening as per the Armstrong-Frederick (1966) model. The parameters of the model were calibrated to represent the low-carbon Grade 50 steel (A992) commonly used in United States construction (see Elkady and Lignos 2015 for values). It is relevant to note here that this constitutive model was monotonically hardening, which implies that softening-induced mesh convergence was not encountered. Fixed boundary conditions were applied at one end of the column, and axial forces and lateral displacements were applied at the other. Depending on the test problem (Table 1), axial force was either (1) applied simultaneously (i.e., proportionally) with the lateral displacement or (2) in advance of the lateral displacement and then held constant during application of the lateral displacement. In each case, the axial force was a follower force, meaning that it did not induce additional *P*-delta moments about the fixed end. Elkady and Lignos (2015) extensively validated models constructed with this protocol and determined that they reproduced not only the load-deformation response but also the local response (including buckled shapes and strain distributions) with high accuracy. Residual stresses were not considered in the CFE simulations or in the fiber formulations discussed subsequently; this followed observations by Newell and Uang (2006) and Elkady and Lignos (2012), who determined that residual stresses do not significantly affect the response of compact wide-flanged sections, which undergo yielding prior to local buckling.

As a representative example, Fig. 3(a) shows a specimen identical with test problem 42 [simulated by the FE model in Fig. 3(b)] at the same deformation level as the FE model; the agreement in the deformed shape, as well a similar correspondence between the load deformation plots in Fig. 3(c) indicates the fidelity of the simulation. Validated in this manner, the results from the FE models may be considered proxies for true responses for the purpose of developing and evaluating the line-element-based model. The following subsections summarize specific information (in addition to the load-deformation curves) that was recovered from the FE models and its implications for the nonlocal formulation.

Localization Length (Characteristic Length for Nonlocal Formulation)

Physical length scales, associated with localization phenomena (in this case, local buckling), are critical from the standpoint of mitigating mesh dependence through the NFE model. In a generic sense, the localization length denotes the distance over which strains increase accompanied by softening, while the adjacent (nonlocalized regions) unload elastically (i.e., strains decrease) to maintain equilibrium with the softening localized zone. In the context of buckling, the softening does not occur at the continuum scale, because the material at any continuum location hardens monotonically with respect to the continuum strain. Rather, the rotation of the buckling elements (e.g., flange segments) manifests itself as an effective longitudinal strain. Fig. 4(a) (which shows representative simulation results) illustrates the genesis of this strain as it pertains

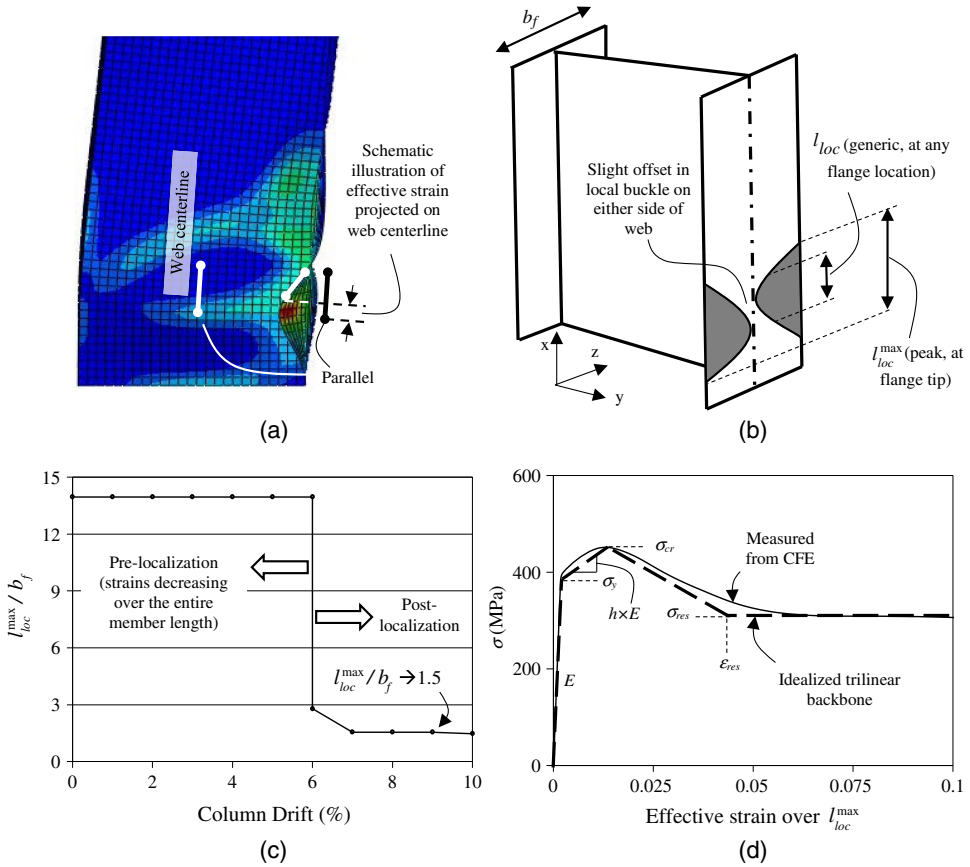

Fig. 4. Quantities derived from CFE simulations: (a) effective or projected strain; (b) spatial distribution of localization length at an arbitrary time instant postlocalization; (c) temporal evolution of flange tip (peak) localized length l_{loc}^{max}; and (d) effective stress–strain relationship measured over l_{loc}^{max} and its idealization through the trilinear backbone of the Ibarra et al. (2005) model (only compression quadrant shown).

to the projection of the flange rotations on the member axis. When the effective stress–strain response was considered at this scale (i.e., in a uniaxial sense over the length of the buckle), the aforementioned softening behavior was observed along with the attendant localization length, within which the projected strains increased and the stresses (also projected along the member axis) decreased. This occurred because flange rotation within this zone diminished the longitudinal component of flange stress, even as the continuum stress itself increased because of material hardening. With this background, the localization length was determined at each loading step of each simulation in order to determine an instantaneous value of the localization length. Furthermore, this instantaneous value of localization length was determined at multiple locations through the width of the flange [i.e., in the z-direction, in Fig. 4(b)]. The process for determining localization length was as follows:

1. At each location (x, z) in the flange [see Fig. 4(b) for a reference coordinate system] the instantaneous effective strain is determined as

$$\varepsilon_{\text{effective}}(x,z) = \frac{|\overrightarrow{\Delta L^{\text{flange}}(x,z)}| - |\overrightarrow{\Delta L^{\text{flange}}(x,z)} \cdot \overrightarrow{\Delta L^{\text{web-centerline}}(x)}|}{|\overrightarrow{\Delta L_0^{\text{web-centerline}}(x)}|} \quad (1)$$

   where $\overrightarrow{\Delta L^{\text{flange}}(x,z)}$ (defined at any location on the flange) is a sufficiently small vector representing the local orientation and length of a line segment on the flange located at (x, z), which represent the initial (undeformed) coordinates; and the vector $\overrightarrow{\Delta L^{\text{web-centerline}}(x)}$ is a similar vector at the centerline of the web located at the same longitudinal coordinate x (for the web, $z = 0$). As such, the numerator on the right-hand side of Eq. (1) represents the effective reduction in length due to rotation of the flange in the local buckle. The denominator $|\overrightarrow{\Delta L_0^{\text{web-centerline}}(x)}|$ represents the magnitude of a corresponding line segment at the web centerline in the undeformed state. These terms are determined numerically at each location, based on the displacements recovered from the CFE simulations. Projection on the deformed web centerline $\overrightarrow{\Delta L^{\text{web-centerline}}(x)}$ rather than the undeformed longitudinal axis eliminates the component of effective strain that arises from bending rotation of the entire cross section without localization.
2. Once the projected strains $\varepsilon_{\text{effective}}(x, z)$ are determined in this manner, strain rates (with respect to analysis-time) at each location $\dot{\varepsilon}_{\text{effective}}(x, z)$ may be determined through numerical differentiation over loading increments.
3. At any instant before the initiation of local buckling, all fibers in the compression flange undergo compression; that is, the strain rate is negative (compressive) throughout the length of the flange. After local buckling, the localized strains result in a contiguous zone within which the projected strain $\dot{\varepsilon}_{\text{effective}}(x, z)$ rate is negative (i.e., the buckling zone), whereas the strain rate outside it is positive (i.e., the unloading zone). Fig. 4(b) illustrates the spatial extent of this localized zone for the simulation shown in Fig. 4(a). Observations were qualitatively similar for all other simulations. As the figure shows, the length of this zone (denoted as l_{loc} at any location along the flange) is the greatest along the flange tip (denoted as $l_{\text{loc}}^{\max}$) and decreases towards the web. Fig. 4(c) shows the temporal evolution of $l_{\text{loc}}^{\max}$. As the figure shows, the term $l_{\text{loc}}^{\max}$ is a constant before localization, indicating that the effective strain $\dot{\varepsilon}_{\text{effective}}(x, z)$ decreases along the entire compression flange because of nonlocalized cantilever bending. Fig. 4(c) shows the evolution of the localized length $l_{\text{loc}}^{\max}$ (versus applied deformation, expressed as percent drift) for the representative simulation. However, the length of this zone drops suddenly at the onset of localization (on average at a column drift angle Δ/L of between 4% and 6%), and remains unchanged thereafter. In the postlocalization phase, the remainder of the compression flange undergoes a net increase in $\dot{\varepsilon}_{\text{effective}}(x, z)$ as it elastically unloads. The value $l_{\text{loc}}^{\max}$ was appropriate from the standpoint of incorporation into the NFE model, since it subsumed the entire localized zone. For all the test problems, $l_{\text{loc}}^{\max}$ was directly proportional to the flange width and relatively insensitive to other model parameters, including moment gradient (which may otherwise be expected to nominally affect the plastic hinge length, and consequently the characteristic length) and axial load, such that the relationship $l_{\text{loc}}^{\max} = 1.5 \times b_f$, in which b_f is the flange width, was an excellent predictor of the localized length. Fig. 4(c) illustrates this for one of the test problems. While the constant 1.5 is specific to this study, it is consistent with the results of Lay (1965), who determined the length of a local buckle in a wide-flanged section in flexure to be approximately 1.5 times the flange width. In a comparable finding, Fell et al. (2010) also determined the length of local buckles in axially compressed W-sections to be in a similar range.

In Figs. 3(b) and 4(a), a portion of the web also deforms to maintain compatibility with the buckling flange. However, localization is not observed in the web [along with the central portion of the flange; see Fig. 4(b)], such that all fibers in this region continue to show monotonic increase in effective stress–strain response until the flange shows localization, at which point elastic unloading occurs. Following this, as discussed in the next section, only the flange was simulated as a softening material in the NFE model; the web was simulated as a monotonically hardening local material.

Fiber Stress–Strain Response

To inform the NFE formulation, the stress–strain response for the localized region of the flange was recovered from the CFE models. Fig. 4(d) illustrates this response. In Fig. 4(d) [and in Fig. 4(a)], the projected strain was determined by integrating $\varepsilon_{\text{effective}}(x, z)$ over the entire length of the localized zone; the longitudinal stress σ was recovered from the finite elements adjacent to the localized zone. Note that the stress–strain response shown in Fig. 4(d) was calculated for the entire width of the flange, rather than for individual fibers (or $z-$ locations). The stress values in the figure represent an average stress through the width. Similarly, the strain was determined by computing the average longitudinal strain over the flange width. Consequently, the curves represent the aggregated response of the entire buckling flange. Characterizing the constitutive response in this manner (rather than for individual fibers through the flange width) was expedient within the scope of the 2D line-element formulation for uniaxial bending, which cannot accommodate variation in stresses or strains in the out-of-plane direction. As expected, the resulting curve shows an initial elastic region followed by a well-defined peak and a negative slope. At increasing deformations, the steepness of the descending branch decreases (i.e., flattens out). This type of postbuckling response is well-documented across various components (Krawinkler et al. 1983; Lee and Stojadinovic 1996; Ikeda and Mahin 1986), and occurs when the destabilizing $P-\delta$ effects within the flange saturate as the buckle amplitude approaches a maximum value. It is relevant that the postpeak response of the fiber shown in Fig. 4(d) is dependent on the gage length (i.e., the localized length) over which strains are measured. As such, the postpeak response is

meaningless without this accompanying length scale. This underscores the importance of retaining this value and incorporating it as the characteristic length in the nonlocal model.

Superimposed on the curve in Fig. 4(d) is a trilinear representation of the constitutive response. Approximating the curvilinear response of the CFE models with this trilinear backbone is judicious because (1) it functionally represents the CFE response with reasonable accuracy, notwithstanding some deviation from it at large postbuckling deformations; (2) it enables the convenient parametrization of key response quantities, such as the peak strain and other quantities indicated in Fig. 4(d), which may be generalized across various configurations/cross sections as discussed subsequently; and (3) multilinear stress–strain or load-deformation relationships are commonly used for component simulation [e.g., see ASCE 41-13 (ASCE 2014)], such that existing implementations of trilinear models may be used without the need for developing a new constitutive model. As an example, the modified Ibarra-Medina-Krawinkler constitutive model (Ibarra et al. 2005), which is currently implemented in OpenSees version 2.5.0, includes a trilinear backbone similar to the one shown in Fig. 4(d). In Fig. 4(d), the trilinear response is defined by six parameters: (1) the elastic modulus E, (2) the yield stress σ_y, (3) the hardening ratio h such that the hardening modulus is $h \times E$, (4) the critical stress corresponding to localization σ_{cr}, and (5) the stress σ_{res}, and (6) the strain ε_{res} that define the onset and height of the residual stress plateau. These are discussed in greater detail in the section describing their calibration and generalization. Based on these parameters, the stress–strain response may be expressed as

$$\sigma = E \cdot \varepsilon \quad \text{for } \varepsilon \le \sigma_y/E \tag{2}$$

$$\sigma = \sigma_y + h \cdot E \cdot (\varepsilon - \varepsilon_y) \quad \text{for } \varepsilon_y < \varepsilon \le \varepsilon_{cr} = \varepsilon_y + (\sigma_{cr} - \sigma_y)/(h \times E) \tag{3}$$

$$\sigma = \sigma_{cr} - (\varepsilon - \varepsilon_{cr}) \cdot (\sigma_{cr} - \sigma_{res})/(\varepsilon_{res} - \varepsilon_{cr}) \quad \text{for } \varepsilon_{cr} < \varepsilon \le \varepsilon_{res} \tag{4}$$

$$\sigma = \sigma_{res} \quad \text{for } \varepsilon > \varepsilon_{res} \tag{5}$$

These equations represent a functional form that requires additional adaptation for the nonlocal formulation (discussed in the subsequent section). Specifically, the nonlocal strain quantity ε^* is derived from the aforementioned functional form, such that ε^* is a spatially averaged total strain (as referenced previously), except that it is invoked only after the attainment of peak stress σ_{cr}. The following section discusses the development of the nonlocal formulation based on these qualitative and quantitative insights. The tensile response of the material [not shown in Fig. 4(d)] is represented as bilinear hardening (as defined by the parameters E, σ_y, and h) without the softening branches.

Implementation of Nonlocal Formulation for Fiber-Based Line Elements

The nonlocal formulation is implemented within the NFE model discussed previously (Fig. 2). To provide context for the mathematical form of the formulation, it is useful to first establish the computational framework within which it was realized. A brief overview follows:

1. Applied incremental loads or displacements or forces (e.g., at the tip of the cantilever in Fig. 2) along with a tangent stiffness matrix were used to calculate a trial incremental nodal displacement vector. This tangent stiffness matrix was computed from local strains from the previously converged step. Although a consistent tangent matrix based on the nonlocal strains (e.g., Jirasek and Patzak 2002) would accelerate convergence, the derivation of such a tangent matrix was outside the scope of this work.
2. The incremental displacement vector (along with displacements from the previously converged load step) was used to determine curvatures and axial strains along the length of each element (i.e., at each Gauss integration point) using shape functions. These were subsequently converted to local fiber strains based on the PSRP assumption.
3. Nonlocal strains were computed at each Gauss point by applying the formulation (discussed subsequently) to local strains (as determined in the previous step) in the neighborhood of that point. Depending on the selected length scale and mesh density, this neighborhood sometimes extended to several adjacent elements. Note that the nonlocal strains were computed only from strains at the same fiber (i.e., z-location) measured over a neighborhood in the longitudinal (i.e., x-direction); in other words, the interaction between fibers at the same cross section was not considered. In fact, since the constitutive response [as shown in Fig. 4(d)] was represented in an average sense for the entire flange (i.e., not considering through-width variations), the flange was represented as a single fiber.
4. The softening constitutive relationship [represented by the trilinear backbone, as shown in Fig. 4(d)] was used to determine stresses in each fiber at each Gauss point; these stresses were integrated to conduct force recovery, i.e., to determine cross-sectional and nodal forces and moments. An appropriate iterative scheme (e.g., Newton-Raphson) was used to eliminate residual nodal forces such that a converged force and displacement vector was obtained and retained for the subsequent load step.

The three key components of this framework are outlined in the following subsections: (1) nonlocal strain definition, (2) softening constitutive relationship, and (3) operational details

Nonlocal Strain Definition

The primary objective of the nonlocal strain measure was to facilitate the introduction of a physical length scale into the constitutive response in order to mitigate mesh dependence. A previously developed formulation (Kolwankar et al. 2017) for single-fiber response was adapted to the fiber formulation, since it had been demonstrated to successfully mitigate mesh dependence and also reproduce strains inside the localized zone. Eqs. (6)–(9) show the expressions for calculating the nonlocal strain ε^*

$$\varepsilon^* = m \cdot \varepsilon^w + (1 - m) \cdot \varepsilon \tag{6}$$

where ε^w = weighted average of strain in the neighborhood of any point

$$\varepsilon^w(x) = \int_{L_c} \alpha(x, \xi) \cdot \varepsilon(x, \xi) \cdot d\xi \tag{7}$$

where $\alpha(x, \xi)$ represents a weighting function defined over length L_c; and ξ is a local variable, such that a bell-shaped weighting function may be generated as

$$\alpha(x, \xi) = \frac{\alpha'(x, \xi)}{\int_{L_c} \alpha'(x, \xi) \cdot d\xi} \tag{8}$$

where

J. Struct. Eng., 2018, 144(10): 04018192

$$\alpha'(x,\xi) = \frac{15}{8 \cdot L_c}\left(1 - \frac{4 \cdot (x-\xi)^2}{L_c^2}\right) \quad \text{for } |x-\xi| \le L_c/2;$$
$$\alpha'(x,\xi) = 0 \quad \text{for } |x-\xi| > L_c/2 \tag{9}$$

The normalizing term $\alpha'(x,\xi)$ prevents spurious alteration of a homogenous strain field. This is termed an "over-nonlocal" formulation (Vermeer and Brinkgreve 1994), which combines the commonly used form of nonlocal strain (usually determined as ε_p^w) and the local strain ε. The parameter m determines the relative contribution of these two components and provides an additional degree of freedom (or parameter) in the model for more accurate simulation of the load-displacement response and strain distributions. For this study, m was selected as 1.5 following the work of Kolwankar et al. (2017); L_c was selected as $1.5 \times b_f$, since it is the best estimate of the physical length scale $l_{\text{loc}}^{\max}$ associated with local buckling, as discussed previously.

Softening Constitutive Relationship

In Fig. 4(d) and the associated discussion, a trilinear curve was used to represent the buckling-induced softening response in compression, and a bilinear curve was used to represent the tensile yielding response. This resulted in six parameters, which may be calibrated to provide the best fit with the curve obtained for a particular geometric/loading configuration, i.e., for each of the test problems listed in Table 1. While this type of case-by-case calibration may potentially result in the best possible fit with test data, it cannot be generalized to different members or configurations. Consequently, for all six parameters in the constitutive model, best practices were developed to facilitate general calibration:

1. The parameters E, σ_y, and h may be used directly from the uniaxial material tensile coupon (or specified) data, because they do not pertain to localization. In case h cannot be conveniently determined from coupon tests, a value of 0.05 is recommended, following the work of Elkady and Lignos (2015).
2. The critical stress σ_{cr} at which local buckling initiates can be approximated by the following equation:

$$\sigma_{cr} = 1.1 \times \sigma_u - 2.17\frac{b_f}{2t_f} \tag{10}$$

   where σ_u is the ultimate strength of the material; and $b_f{:}2t_f$ is the flange width–thickness ratio. The expression in Eq. (10) is a regressed relationship (against data from all the CFE simulations, with $R^2 = 0.95$), which reflects the dependence of the flange local buckling strength on the width-thickness ratio. Various similar relationships were trialed (and researched in the literature), and the influence of other parameters, including web slenderness and material hardening, was examined. It was determined that the flange width–thickness ratio is the dominant parameter controlling local buckling. The dominance of $b_f{:}2t_f$ in controlling local buckling is well-documented, such that it is routinely used as a basis for member selection and design (AISC 2016). Furthermore, the use of $b_f{:}2t_f$ as the sole parameter is supported by the work of Hartloper and Lignos (2017), because for hot-rolled cross sections, $b_f{:}2t_f$ and the web slenderness ratio $h{:}t_w$ are well-correlated.
3. Expressions for the parameters σ_{res} and ε_{res}, which define the descending branches of the softening relationship, should be regressed as functions of $b_f{:}2t_f$ [in a manner similar to the procedure outlined for σ_{cr}, $R^2 = 0.56$, and 0.98 for Eqs. (11) and (12), respectively]:

$$\varepsilon_{res} = 0.15 - 0.014\frac{b_f}{2t_f} \ge \frac{\sigma_y}{E} + \frac{\sigma_{cr} - \sigma_y}{h \times E} \tag{11}$$

$$\sigma_{res} = \sigma_y - 1.44\frac{b_f}{2t_f} \ge 0 \tag{12}$$

As with σ_{cr}, the flange width–thickness ratio was the dominant quantity controlling these parameters as well. Note that the aforementioned approaches for estimating these parameters are provided mainly for convenience and do not materially impact the nonlocal formulation itself. More refined estimates or approaches may be used if additional data is available for specific materials or configurations (e.g., Torabian and Schafer 2014).

Operational Details

In addition to the aforementioned two main components of the formulation, some other details are important from an operational standpoint. These include:

- Providing sufficient mesh density over the localized zone to prevent localization within one element. This is discussed in greater detail in a subsequent section.
- Introduction of perturbations [in the form of slightly reduced area (2% less than the nominal flange area)] at fixed intervals along its length. The interval was selected to be on the order of b_f to reflect imperfection patterns measured by Elkady and Lignos (2015) and used in the CFE simulations. These are usually not activated in simulations with moment gradients but are introduced to trigger localization in simulations with constant moment.
- Additional operational processes (that did not influence the final solutions) were adopted to aid convergence. These were: (1) nonlocal strain averaging was invoked only after the peak stress σ_{cr} was attained; (2) nonlocal averaging was conducted for the total rather than the plastic strain; and (3) the unloading slope (which was activated in the regions outside the localized zone) was assumed equal to the elastic modulus E.

The line-element formulation as described in this section was used to simulate all the test problems shown in Table 1 and in two experiments previously conducted by Lignos et al. (2016). Results of these simulations, when compared to corresponding CFE or experimental results, may be used to examine efficacy of the proposed approach, especially as it pertains to the mesh sensitivity of the load-deformation response and the deformation distribution. This is discussed in the next section.

Results and Discussion

Each of the test problems summarized in Table 1 was simulated through the line-element-based model and the nonlocal formulation, implemented as outlined in the preceding section. Selected results from these simulations are illustrated in Figs. 5–7. Figs. 5(a–i) compare the efficacy of conventional fiber-based elements and the NFE approach for simulating the load-deformation response (as determined from the CFE). Figs. 5(a–c) show load-deformation curves determined from the conventional fiber-based line-element models for three loading cases (with $P/P_y = 0$, 0.2, and 0.5 and $M{:}V =$ 4500 mm, all for W24X146, i.e., test problems 17–19). The conventional fiber models utilized the trilinear backbone model and its attendant calibration [as outlined in the preceding section and Eqs. (10)–(12)]. However, they did not include the nonlocal formulation and the associated length scale. The load-deformation curves from these models were overlaid on their counterparts from the CFE simulations, which may be considered objective benchmark

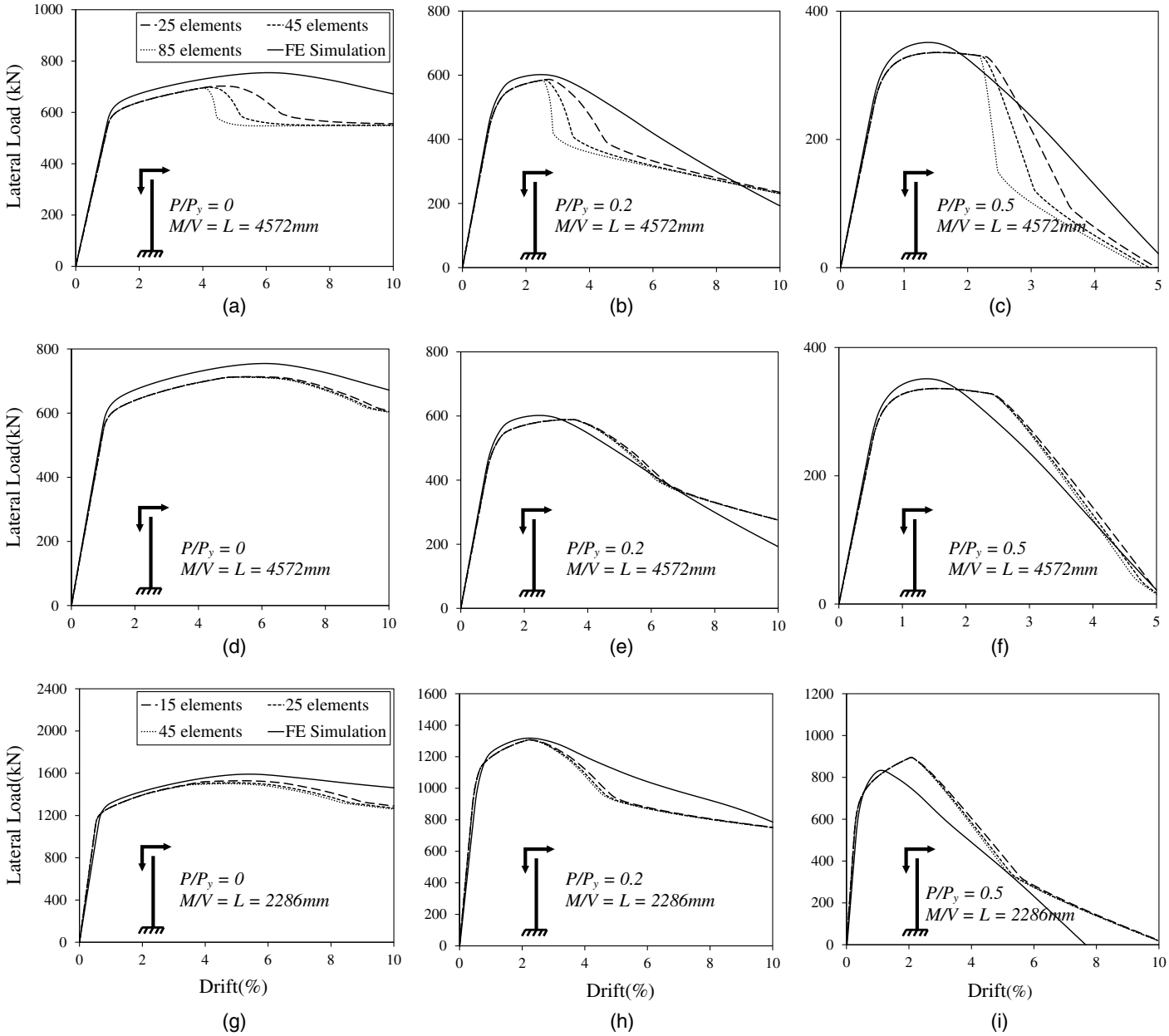

Fig. 5. Representative load-displacement curves from select test problems with W24X146: (a–c) conventional fiber approach; and (d–i) nonlocal fiber approach.

responses. The line-element-based models included 25, 45, and 85 elements in order to examine the influence of mesh-density on the load deformation curve. From Figs. 5(a–c), the following observations may be made:

- As expected, an increase in axial load ratio resulted in a decrease in peak strength and steeper (i.e., more rapidly decreasing) postpeak response.
- The conventional fiber models reproduced peak strength accurately, since they were able to capture $P-M$ interactions and utilize estimates of σ_{cr} [Eq. (10)] that reflect true response with good accuracy. However, the limitations of the conventional approach became apparent during the postpeak response, in which significant mesh-sensitivity was observed along with deviation from the CFE response.

Figs. 5(d–i) are similar to Figs. 5(a–c), except that they show results from the NFE models with the nonlocal formulation developed in this study. These figures also show results for three additional load cases, corresponding to $M{:}V = 2250$ mm (test problems 20–22). An examination of the figures reveals the following:

- As with the conventional fiber models, the NFE models replicated the prepeak load-deformation response (of the CFE models) with reasonable accuracy. In addition, the NFE models were able to track postpeak response for all the loading cases with good accuracy, even to large drifts (approximately 10%), which indicates that the approach effectively simulates $P-M$ interaction and moment gradient effects. A similar agreement was observed for proportionally loaded specimens (not shown in Fig. 5). Importantly, this response was mesh-independent, such that the load deformation curves corresponding to the different element sizes were virtually coincident.
- In the latter stages of response, the load from the CFE simulations dropped somewhat uniformly, whereas that from the NFE stabilized slightly; this is particularly notable in Figs. 5(h and i).

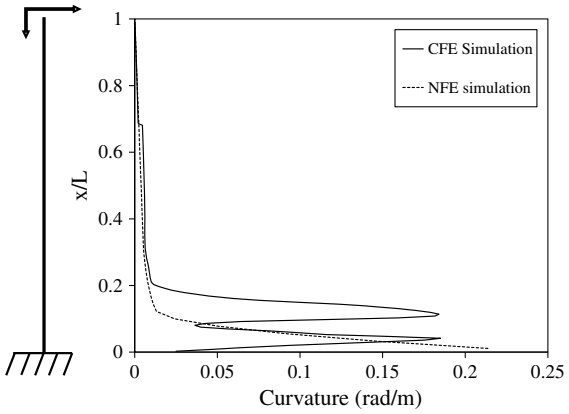

Fig. 6. Post localization curvature profile for W24X146 with $P/P_y = 0.2$ from CFE and NFE simulations at 8% drift.

For Fig. 5(h), this appears to be an artifact of the Ibarra et al. (2005) implementation of the trilinear backbone, which had an ideally flat residual stress capacity; this may be suitably overcome by prescribing a constitutive relationship that more closely follows the measured response. In Fig. 5(i), the peak load itself is mischaracterized by the nonlocal approach. This configuration had a high axial load $P/P_y = 0.5$, suggesting that the calibrated parameters of the trilinear backbone (specifically σ_{cr}) did not reflect the peak stress associated with flange local buckling under a combination of high axial and flexural loads.

- The agreement in Figs. 5(d–i) is notable, given that neither the nonlocal formulation, nor the constitutive parameters were back calibrated (or refined) based on the global load-deformation curve. In fact, the constitutive parameters (which were defined for local flange stress–strain response) were determined from Eqs. (10)–(12). This indicates that the approach upscales fiber-level postpeak softening response to obtain global response in

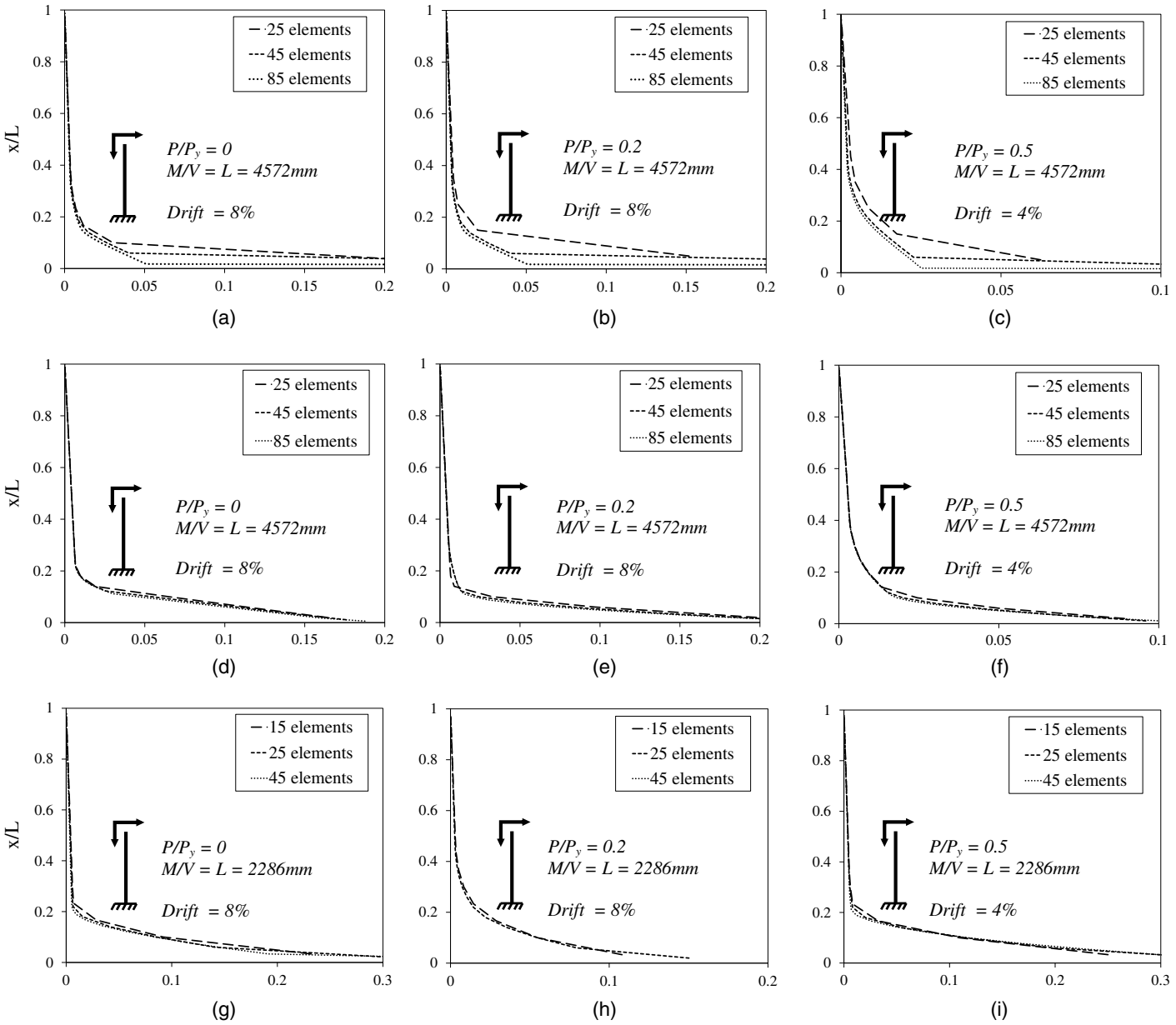

Fig. 7. Representative curvature distribution from select test problems with W24X146: (a–c) conventional fiber approach; and (d–i) nonlocal fiber approach.

a reasonable manner. However, some discrepancies were noted as well, especially in the latter stages of deformation.

A similar analysis of the deformation patterns simulated by the line-based nonlocal model (relative to the CFE model) requires some discussion to contextualize the results. Fig. 6 shows a representative plot of a postlocalization curvature profile (for test problem 20 at 8% drift) as determined from the CFE simulation. The curvatures were back-calculated by dividing the projected strains at the extreme fibers [as determined from Eq. (1)] by the section depth. Overlaid on this plot was the curvature profile (forthe same test problem and loading step), as recovered directly from the NFE model (with 45 elements). Observing the two curves, it is noteworthy that the curvature profile from the CFE model resembles a double-plateau shape, which arose from the double-plateau shape of the projected flange strain profile discussed previously in addition to the slight stagger between the flange buckle on either side of the web [Fig. 4(b)]. In its current form, the NFE model was unable to capture this response, which was the result of the complex buckling mode. As a result, the curvature localized (as one peak) in the region closest to the support, in which the moment was highest. With this background, the efficacy of the line-element-based model to simulate deformation/strain distribution was assessed in the context of its ability to characterize the length of the localized zone and the peak curvature in a mesh-independent manner. More specifically, although the curvature values as determined by the NFE simulations were not meaningful in an absolute sense, they could be integrated over the localized zone to provide a sense of the overall deformation in the localized zone. Perhaps more importantly, the NFE-inferred curvature could be used to assess local damage in a relative sense across different beam–columns with local buckling. With this background, Figs. 7(a–i) show snapshots of the longitudinal curvature profiles for the same test problems as shown in Figs. 5(a–i). To examine mesh-sensitivity in the line-element model, results are shown from simulations with various element sizes. Figs. 7(a–c) show results from a conventional fiber-based line element, without the nonlocal formulation. In all cases, the main observations are essentially similar to that for the load deformation curve. Specifically, the conventional fiber model exhibited mesh dependence such that, near the support, the curvature profile was entirely controlled by mesh density, with localization occurring in exactly one element. Fig. 7(a) indicates this specifically, although a similar phenomenon was also observed in Figs. 7(b and c). This caused significant variation in the curvatures at any point within this zone. For purposes of illustration, this variation is indicated in Fig. 7(a) for $x{:}L = 0.05$. The implication is that these results cannot be interpreted meaningfully. However, the NFE-based model mitigated the mesh dependence by smearing the localization length over several elements. As a result, the curvature profile (especially near the support) was controlled by the physical length scale rather than the mesh size. Fig. 8 provides further examination of the effect of mesh size, plotting the curvatures determined from NFE-based models at a distance $L_c/2$ from the cantilever support, i.e., at the center of the localized zone, against L_c/element size. These curvatures were recovered at displacements well into the postpeak or localized regime for the three test problems. From the figure, two observations may be made. First, as the mesh size is refined (i.e., L_c/element size is increased), the curvatures converge, which indicates that the nonobjectivity is effectively mitigated. For a conventional local formulation, the strains become unbounded as element size is reduced. For the test problems shown (results for all other test problems are similar) this convergence was observed at approximately $L_c/\text{element size} = 10$, which suggests an appropriate mesh refinement for accurate simulation of postpeak response. As a point of reference, even with this degree of refinement, the NFE cantilever model requires roughly 1/20 to 1/50 the time

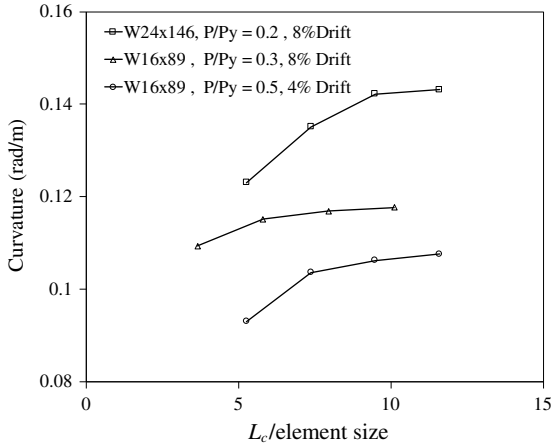

Fig. 8. Curvatures at a distance of $L_c/2$ from support determined from NFE models for various discretizations.

(approximately 30 s) to execute as compared to the counterpart CFE model (approximately 1,200 s). Note that this estimate may vary significantly depending upon the computer hardware, other features of the software implementation (e.g., parallelization), and the complexity of the structure being analyzed. As a result, this estimate is provided only to indicate that the NFE model does provide a substantial decrease in computational time for a set of problems. Notwithstanding the limitations of the curvature measure as illustrated in Fig. 6, the NFE-based estimates of curvature offer an improvement over the conventional fiber model because of their mesh-independence, which implies that they may be interpreted more meaningfully to assess damage.

As an additional validation exercise, the NFE models were used to predict the response of two experiments on beam–columns (W16X89 with $P/P_y = 0.3$ and 0.5) conducted by Lignos et al. (2016). Fig. 9(a) shows one of these experiments being conducted; Figs. 9(b and c) overlay load-deformation curves from these experiments on the corresponding predictions from the NFE models with three mesh densities. The predictions were conducted in a blind sense, meaning that only the configurational parameters of the test specimen and setup were used to inform the fiber-based model. To recapitulate, the characteristic length L_c was calculated as $1.5 \times b_f$, and the parameters of the softening constitutive model were calculated from Eqs. (10)–(12); note that these estimates were not influenced by the experimental data. The figures indicate that when calibrated as per the guidelines provided, the NFE models reproduced the experimental curves (including the postpeak response) with high accuracy. The results are encouraging for the following reasons: (1) the NFE models were not compromised by the mesh density, and thereby overcame the main limitation of the conventional fiber-based approach, and (2) they were able to capture differences in postpeak response across the two experiments with different axial loads by integrating fiber-scale constitutive response rather than calibration to large-scale tests, thereby retaining the key strength of the fiber approach.

Summary, Conclusions, and Limitations

This article presents a nonlocal fiber-element based framework for simulating 2D beam–column elements, focused on rolled steel sections susceptible to local buckling-induced softening. The approach overcomes the problem of nonobjectivity (i.e., mesh dependence) which is usually a limitation of fiber-based models,

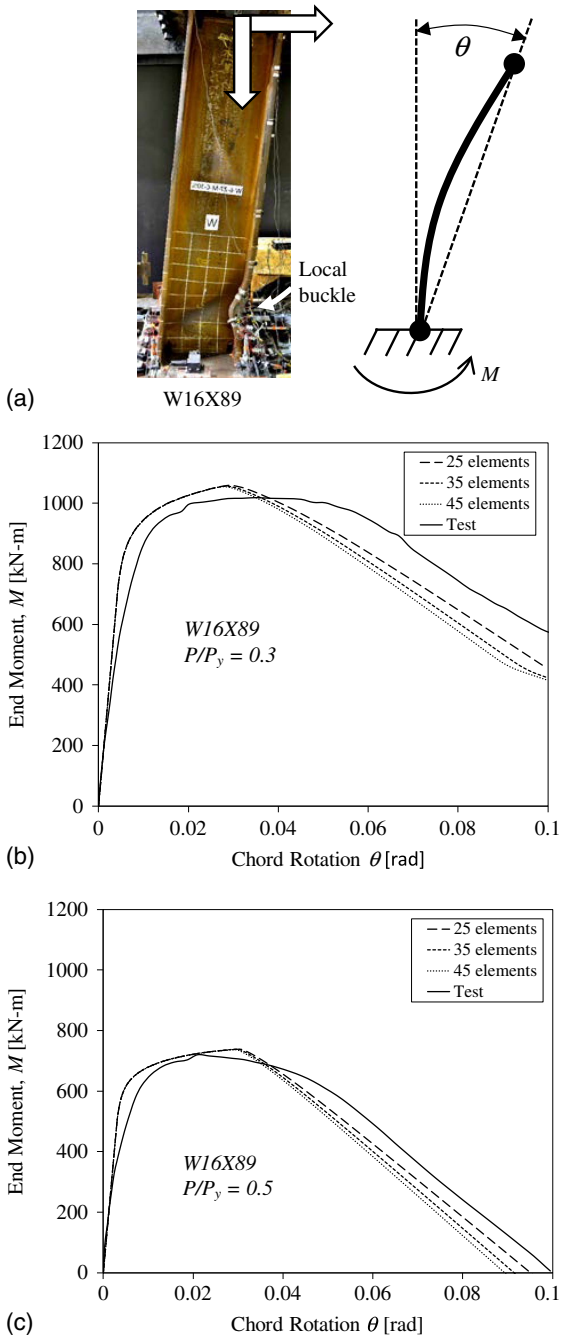

Fig. 9. Prediction of tests results by Lignos et al. (2016): (a) test setup and illustration of plotted quantities; results from test and NFE model for W16X89 with (b) $P/P_y = 0.3$; and (c) $P/P_y = 0.5$.

while retaining attractive features of fiber-based models such as the ability to capture $P - M$ interaction, the initiation of plasticity at arbitrary locations, and its spread. The approach provides a computationally efficient alternative to continuum finite element modeling, which is currently the only viable approach for simulating local buckling-induced softening in an objective manner. To achieve this, the proposed approach upscales recent work that demonstrated the use of a nonlocal formulation to simulate geometric nonlinearity-induced softening (i.e., postbuckling response) in a single fiber to a complete frame element. The implementation in the open source software OpenSees is discussed, and guidelines for the calibration and execution of the framework are outlined. The approach is informed by a comprehensive set of continuum finite element simulations that examine a range of parameters, including cross-sectional shape, moment gradient, and axial load ratio.

The main elements of this approach include (1) estimation of the physical length scale associated with local buckling; (2) estimation of the effective postbuckling constitutive response at the fiber level; (3) idealized representation of this response through a softening constitutive model, which utilizes a nonlocal strain formulation; (4) numerical implementation within OpenSees such that the user may designate physical beams or columns as single members, with the following inputs: (a) length scale, (b) parameters for the softening constitutive relationship, and (c) desired mesh density; and (5) guidelines for calibration/selection of these inputs.

The implemented approach is used for prediction of the CFE simulations (both load-deformation response and curvature distribution) and experimental results. The results are encouraging in that the approach successfully mitigates mesh dependence across a range of configurational parameters. In addition, it effectively simulates the effect of $P - M$ interactions and moment gradient on load-deformation as well as deformation amplification within the localized zone. The latter is particularly attractive in contrast to other approaches for mitigation of nonobjectivity in frame elements, in which the softening response is adjusted in concert with the mesh size. As a result, it may be used for assessment of downstream damage states through the use of appropriate damage/fracture models (e.g., Smith et al. 2017). The use of nonlocal formulations to simulate buckling-induced (or more generally, geometric nonlinearity-induced) softening is nascent, and as such the overall framework is still under development. Consequently, the framework has several limitations which must be considered in its use and for future development. From a physical standpoint, the framework only addresses one form of localization and softening, that which is due to local buckling. Other forms, such as lateral-torsional or distortional buckling (Yu and Schafer 2006) are not currently within its scope. Similarly, three-dimensional response modes of biaxial bending or torsion are not considered. Cyclic loading is similarly not addressed; this is possibly the most important area of future work.

Some aspects of response (e.g., participation of the web in the local buckling mode) were disregarded in favor of simplicity. Similarly, the local curvatures obtained from the NFE approach may be interpreted only in a relative sense, given its inability to reproduce the double-plateau curvature profile corresponding to local buckling. Moreover, since the parameters for the constitutive model are calibrated to provide best fit with the data, caution should be exercised in generalizing these to different members or configurations. Finally, the approach inherits some structural limitations of the fiber approach, such as the plane-sections-remain-plane assumption. Notwithstanding this, the proposed approach establishes the viability of using nonlocal formulations to simulate geometric nonlinearity-induced softening and localization in an objective manner. The observed accuracy of the approach (especially for the blind predictions of the experiments) is encouraging in itself. Perhaps most importantly, the approach provides a generic framework which may be extended to simulate other aspects of physical response by overcoming the limitations outlined previously.

Acknowledgments

The work was supported by the National Science Foundation (Grant No. CMMI 1434300) and graduate fellowships from the University of California, Davis. The findings and opinions presented in this paper are entirely those of the authors.

References

AISC. 2016. *Seismic provisions for structural steel buildings*. AISC 341-16. Chicago: AISC.

Armstrong, P. J., and C. O. Frederick. 1966. *A mathematical representation of the multiaxial Bauschinger effect*. Berkeley, CA: Berkeley Nuclear Laboratories.

ASCE. 2014. *Seismic evaluation and retrofit of existing buildings*. ASCE 41-13. Reston, VA: ASCE.

Bazant, Z. 1976. "Instability, ductility, and size effect in strain-softening concrete." *J. Eng. Mech.* 102 (2): 331–344.

Bazant, Z. P., and M. Jirasek. 2002. "Nonlocal integral formulations of plasticity and damage: Survey of progress." *J. Eng. Mech.* 128 (11): 1119–1149. https://doi.org/10.1061/(ASCE)0733-9399(2002)128:11(1119).

Bazant, Z. P., and B. H. Oh. 1983. "Crack band theory for fracture of concrete." *Mat. Struct.* 16 (3): 155–177. https://doi.org/10.1007/BF02486267.

Bazant, Z. P., and J. Planas. 1998. *Fracture and size effect in concrete and other quasibrittle materials*. Boca Raton, FL: CRC Press.

Coleman, J., and E. Spacone. 2001. "Localization issues in force-based frame elements." *J. Struct. Eng.* 127 (11): 1257–1265. https://doi.org/10.1061/(ASCE)0733-9445(2001)127:11(1257).

Computers and Structures. 2016. *ETABS: Integrated building design software: Users guide*. Berkeley, CA: Computers and Structures.

Dides, M. A., and J. C. De la Llera. 2005. "A comparative study of concentrated plasticity models in dynamic analysis of building structures." *Earthquake Eng. Struct. Dyn.* 34 (8): 1005–1026. https://doi.org/10.1002/eqe.468.

di Prisco, M., and J. Mazars. 1996. "Crush-crack: A nonlocal damage model for concrete." *Mech. Cohesive Frictional Mater.* 1 (4): 321–347. https://doi.org/10.1002/(SICI)1099-1484(199610)1:4<321::AID-CFM17>3.0.CO;2-2.

Elkady, A., and D. G. Lignos. 2012. "Dynamic stability of deep slender steel columns as part of special MRFs designed in seismic regions: Finite element modeling." In *Proc., First Int. Conf. on Performance-Based and Life-Cycle Structural Engineering (PLSE)*. Hong Kong.

Elkady, A., and D. G. Lignos. 2015. "Analytical investigation of the cyclic behavior and plastic hinge formation in deep wide-flange steel beam-columns." *Bull. Earthquake Eng.* 13 (4): 1097–1118. https://doi.org/10.1007/s10518-014-9640-y.

Engelen, R. A. B., M. G. D. Geers, and F. P. T. Baaijens. 2003. "Nonlocal implicit gradient enhanced elasto-plasticity for the modeling of softening behavior." *Int. J. Plast.* 19 (4): 403–433. https://doi.org/10.1016/S0749-6419(01)00042-0.

Fell, B. V., A. M. Kanvinde, and G. G. Deierlein. 2010. *Large-scale testing and simulation of earthquake induced ultra low cycle fatigue in bracing members subjected to cyclic inelastic buckling*. Technical Rep. No. 172. Stanford, CA: Stanford Univ.

FEMA. 2012. *Seismic performance assessment of buildings*. FEMA P-58. Washington, DC: FEMA.

Fogarty, J., and S. El-Tawil. 2015. "Collapse resistance of steel columns under combined axial and lateral loading." *J. Struct. Eng.* 142 (1): 04015091. https://doi.org/10.1061/(ASCE)ST.1943-541X.0001350.

Hamburger, R. O., H. Krawinkler, J. O. Malley, and S. M. Adan. 2009. *Seismic design of steel special moment frames: A guide for practicing engineers*. NEHRP Seismic Design Technical Brief No. 2. Gaithersburg, MD: NIST.

Hartloper, A., and D. Lignos. 2017. "Updates to the ASCE-41-13 provisions for the nonlinear modeling of steel wide-flange columns for performance-based earthquake engineering." In *Proc., Eurosteel 2017*, Copenhagen, Denmark.

Ibarra, L. F., and H. Krawinkler. 2005. *Global collapse of frame structures under seismic excitations*. Technical Rep. No. 152. Stanford, CA: Stanford Univ.

Ibarra, L. F., R. A. Medina, and H. Krawinkler. 2005. "Hysteretic models that incorporate strength and stiffness deterioration." *Earthquake Eng. Struct. Dyn.* 34 (12): 1489–1511. https://doi.org/10.1002/eqe.495.

Ikeda, K., and S. A. Mahin. 1986. "Cyclic response of steel braces." *J. Struct. Eng.* 112 (2): 342–361. https://doi.org/10.1061/(ASCE)0733-9445(1986)112:2(342).

Jirásek, M., and B. Patzak. 2002. "Consistent tangent stiffness for nonlocal damage models." *Comput. Struct.* 80 (14–15): 1279–1293. https://doi.org/10.1016/S0045-7949(02)00078-0.

Jirásek, M., and S. Rolshoven. 2003. "Comparison of integral-type nonlocal plasticity models for strain-softening materials." *Int. J. Eng. Sci.* 41 (13–14): 1553–1602. https://doi.org/10.1016/S0020-7225(03)00027-2.

Khaloo, A. R., and S. Tariverdilo. 2002. "Localization analysis of reinforced concrete members and softening behavior." *J. Struct. Eng.* 128 (9): 1148–1157. https://doi.org/10.1061/(ASCE)0733-9445(2002)128:9(1148).

Khaloo, A. R., and S. Tariverdilo. 2003. "Localization analysis in softening RC frame structures." *Earthquake Eng. Struct. Dyn.* 32 (2): 207–227. https://doi.org/10.1002/eqe.220.

Kolwankar, S. S., A. M. Kanvinde, M. Kenawy, and S. Kunnath. 2017. "A uniaxial nonlocal formulation for geometric nonlinearity-induced necking and buckling localization in a steel bar." *J. Struct. Eng.* 143 (9): 04017091. https://doi.org/10.1061/(ASCE)ST.1943-541X.0001827.

Krawinkler, H., M. Zohrei, B. Lashkari-Irvani, N. G. Cofie, and H. Hadidi-Tamjed. 1983. *Recommendations for experimental studies on the seismic behavior of steel components and materials*. Technical Rep. No. 61. Stanford, CA: Stanford Univ.

Lay, M. G. 1965. *Some studies of flange local buckling in wide flange shapes*. Fritz Engineering Laboratory, Rep. No. 297.10. Bethlehem, PA: Lehigh Univ.

Lee, K., and B. Stojadinovic. 1996. "A plastic collapse method for evaluating rotation capacity of full-restrained steel moment connections." *Theor. Appl. Mech.* 35 (1–3): 191–214. https://doi.org/10.2298/TAM0803191L.

Lignos, D., J. Cravero, and A. Elkady. 2016. "Experimental investigation of the hysteretic behavior of wide-flange steel columns under high axial load and lateral drift demands." In *Proc., 11th Pacific Steel Conf.* Shanghai, China.

Newell, J. D., and C. M. Uang. 2006. *Cyclic behavior of steel columns with combined high axial load and drift demand*. Rep. No. SSRP-06/22. San Diego: Univ. of California.

NIST. 2010. *Nonlinear structural analysis for seismic design*. NEHRP Seismic Design Technical Brief No. 4. Gaithersburg, MD: NIST.

Pugh, J. S., L. N. Lowes, and D. E. Lehman. 2015. "Nonlinear line-element modeling of flexural reinforced concrete walls." *Eng. Struct.* 104: 174–192. https://doi.org/10.1016/j.engstruct.2015.08.037.

Salehi, M., and P. Sideris. 2017. "Refined gradient inelastic flexibility-based formulation for members subjected to arbitrary loading." *J. Eng. Mech.* 143 (9): 04017090. https://doi.org/10.1061/(ASCE)EM.1943-7889.0001288.

Shuttle, D. A., and I. M. Smith. 1988. "Numerical simulation of shear band formation in soils." *Int. J. Numer. Anal. Methods Geomech.* 12 (6): 611–626. https://doi.org/10.1002/nag.1610120604.

Sideris, P., and M. Salehi. 2016. "A gradient inelastic flexibility-based frame element simulation." *J. Eng. Mech.* 142 (7): 04016039. https://doi.org/10.1061/(ASCE)EM.1943-7889.0001083.

Smith, C. M., A. M. Kanvinde, and G. G. Deierlein. 2017. "A local criterion for ductile fracture under low-triaxiality axisymmetric stress states." *Eng. Fract. Mech.* 169: 321–335. https://doi.org/10.1016/j.engfracmech.2016.10.011.

Spacone, E., and F. C. Filippou. 1996. "Fibre-beam column model for nonlinear analysis of R/C frames. Part I: Formulation." *Earthquake Eng. Struct. Dyn.* 25 (7): 711–725. https://doi.org/10.1002/(SICI)1096-9845(199607)25:7<711::AID-EQE576>3.0.CO;2-9.

Torabian, S., and B. W. Schafer. 2014. "Role of local slenderness in the rotation capacity of structural steel members." *J. Constr. Steel Res.* 95: 32–43. https://doi.org/10.1016/j.jcsr.2013.11.016.

Valipour, H., and S. Foster. 2009. "Nonlocal damage formulation for a flexibility-based frame element." *J. Struct. Eng.* 135 (10): 1213–1221. https://doi.org/10.1061/(ASCE)ST.1943-541X.0000054.

Vermeer, P. A., and R. B. J. Brinkgreve. 1994. "A new effective non-local strain measure for softening plasticity." In *Proc., Localization and bifurcation theory for soil and rocks*, 89–100. Rotterdam, Netherlands: Balkema.

Wu, S., and X. Wang. 2010. "Mesh dependence and nonlocal regularization of one-dimensional strain softening plasticity." *J. Eng. Mech.* 136 (11): 1354–1365. https://doi.org/10.1061/(ASCE)EM.1943-7889.0000184.

Yu, C., and B. W. Schafer. 2006. "Simulation of cold-formed steel beams in local and distortional buckling with applications to the direct strength method." *J. Constr. Steel Res.* 63 (5): 581–590. https://doi.org/10.1016/j.jcsr.2006.07.008.

Zhang, G., and K. Khandelwal. 2016. "Modeling of nonlocal damage-plasticity in beams using isogeometric analysis." *Comput. Struct.* 165: 76–95. https://doi.org/10.1016/j.compstruc.2015.12.006.